Mon. Not. R. Astron. Soc. **270,** 641–649 (1994)

The submillimetre structure of the starburst nucleus in M82: a diffraction-limited 450-μm map

D. H. Hughes,[1] W. K. Gear[2] and E. I. Robson[3]

[1] *Astrophysics, Nuclear Physics Laboratory, Oxford University, Keble Road, Oxford OX1 3RH*
[2] *Royal Observatory, Blackford Hill, Edinburgh EH9 3HJ*
[3] *Joint Astronomy Centre, 660 N. A'ohōkū Place, University Park, Hilo, Hawaii 96720, USA*

Accepted 1994 May 5. Received 1994 May 3; in original form 1994 March 24

ABSTRACT

A diffraction-limited continuum map at 450 μm of the central 90×90 arcsec^2 (~ 1.5-kpc diameter) region of the nearby starburst galaxy M82 is presented. These data from the 15-m JCMT represent the highest resolution study (~ 9-arcsec HPBW) yet carried out at submillimetre wavelengths of the thermal reradiated emission from dust in M82. The first continuum observations at 2 mm made at the NRAO 12-m are also presented. The 450-μm data show a double-peaked structure, similar to that observed in various molecular line transitions and 10–30 μm continuum maps. The variation in source size with wavelength and a major-axis intensity profile are consistent with emission from a cooler and larger scale component of the mid-IR dust torus. A spur of thermal emission, similar to that observed in Hα and X-ray emission, is detected extending southwards from the south-western peak. An integrated 450-μm flux density of 41 ± 6.0 Jy is measured. When corrected for free–free emission, the FIR–millimetre continuum is well fitted by optically thin emission from an isothermal population ($T = 48$ K) of dust grains with an emissivity index $\beta = 1.3$.

Key words: galaxies: active – galaxies: individual: M82 – galaxies: ISM – galaxies: nuclei – galaxies: starburst – radio continuum: galaxies.

1 INTRODUCTION

During the last 10^7 years, the nearby irregular galaxy M82 (NGC 3034) has experienced a massive nuclear starburst. Observational evidence for this explosive event has been found in the high far-infrared (FIR) luminosity (Telesco & Harper 1980), together with strong CO emission (Lo et al. 1987; Nakai et al. 1987; Loiseau et al. 1988; Tilanus et al. 1991), extended X-ray emission (Watson, Stanger & Griffiths 1984) and Hα emission (Axon & Taylor 1978; Bland & Tully 1988), a disturbed optical structure (Burbidge, Burbidge & Rubin 1964), the existence of a galactic superwind (McCarthy, Heckman & van Breugel 1987) and ~ 50 compact radio sources identified as supernova remnants by Kronberg, Biermann & Schwab (1985), Huang et al. (1994) and Muxlow et al. (1994).

At optical wavelengths, the edge-on orientation of M82 to our line of sight proves to be a disadvantage, as the active starburst nucleus is heavily obscured. At IR to millimetre wavelengths, however, the galaxy becomes essentially transparent, allowing the study of both the nuclear emission and the outflowing material perpendicular to the galactic plane. The intense star-forming activity is restricted to the central 1 kpc (O'Connell & Mangano 1978). H I (Weliachew, Fomalont & Greisen 1984) and CO observations (e.g. Lo et al. 1987) show that the same central region contains a large double-lobed structure which has been interpreted as a molecular ring. Interior to this ring, IR data reveal a stellar bar in addition to a dusty mid-IR torus (Rieke et al. 1980; Telesco et al. 1991).

Although submillimetre maps of the central 1 kpc in M82 have previously been made at 800 μm and 1.1 mm (Hughes, Gear & Robson 1990, hereafter Paper I) and at 450 μm (Smith et al. 1990), none of these has had sufficient resolution or sensitivity to provide a useful comparison with other IR–millimetre data (e.g. Dietz et al. 1989; Krügel et al. 1990; Carlstrom & Kronberg 1991; Telesco et al. 1991).

The proximity of M82 ($D = 3.25$ Mpc: Tammann & Sandage 1968) provides the opportunity to study in detail the relationship between the ionized, molecular and atomic gaseous phases of the interstellar medium (ISM), the dust distribution and the stellar content of an extragalactic star-forming region. In this paper we describe the first diffraction-limited 450-μm mapping observations, which trace the distribution of thermal emission from dust without contamination from free–free emission and opacity effects.

2 OBSERVATIONS

2.1 Submillimetre mapping

Diffraction-limited 450-μm observations of M82 were made using the ^{3}He bolometer UKT14 (Duncan et al. 1990) and a focal-plane aperture of 27 mm. The data were obtained at the James Clerk Maxwell Telescope (JCMT), Mauna Kea, in 1990 March during a period of extremely stable and transparent atmospheric conditions. The zenith transmission at 450 μm throughout the observations varied between 55 and 66 per cent.

At submillimetre wavelengths it is common practice to make a number of short-integration maps to minimize the influence of variations in the sky transmission and thereby improve the overall signal-to-noise ratio in the final co-added map. Four maps were made in a horizontal coordinate system of the central 68×68 arcsec^2 of M82 using an 'on-the-fly' mapping technique in which the UKT14 aperture was scanned in raster sequence. An east–west chop throw of 150 arcsec, at a frequency of 7.8 Hz, was used to cancel the sky emission. Such large excursions by the secondary mirror produce both an asymmetric beam profile (10.5×7.6 arcsec^2 HPBW with broadening in the chop direction) and significant increases in the uncancelled contribution from the error pattern at 450 μm. A more detailed description of the JCMT beamshape at 450 μm is presented by Richer et al. (1993). Their discussion relates to the surface configuration of the JCMT in 1990 May which was identical to that during our earlier observations presented here.

Each map consisted of a 17×17 azimuth–elevation (az–el) pixel grid with an effective pixel size of 4 arcsec centred on the 2.2-μm nucleus [$\alpha(1950.0) = 09^h\ 51^m\ 43\overset{s}{.}53$, $\delta(1950.0) = 69°\ 55'\ 00\overset{''}{.}7$ (Dietz et al. 1989)]. The integration time per pixel per map was 5 s. Each az–el map was sky-subtracted, despiked and corrected for atmospheric extinction, and then reweighted according to the noise level. A 2D plane was fitted to the background emission in each map and subtracted to remove any remaining baseline gradients before the final reorientation and regridding of the map on to an equatorial coordinate system.

Maps of extended sources made at the shortest submillimetre wavelengths with large chop throws require careful calibration. A map of Mars, a primary calibrator, was made in the same mode as the 450-μm observations of M82 to determine the contribution of emission from the beam error lobes. An integrated flux density of 41 ± 6 Jy was measured in a 60×60 arcsec^2 area centred on the IR nucleus of M82 after an error-lobe correction of 41 per cent had been applied.

The resultant RA–Dec. map (Fig. 1) covers a 90×90 arcsec^2 region with a positional uncertainty of < 3 arcsec and a mean resolution of 9 arcsec or 140 pc at the distance of M82. This 450-μm continuum map covers a larger area than that presented by Smith et al. (1990) and shows significantly more structure due to the greater resolution and sensitivity.

2.2 Millimetre photometry

Continuum observations were made at 3.3 and 2.1 mm using separate SIS receivers at the NRAO 12-m telescope on Kitt Peak in 1993 May. The 2-mm observations represent the first data on M82 at this wavelength. Calibration was

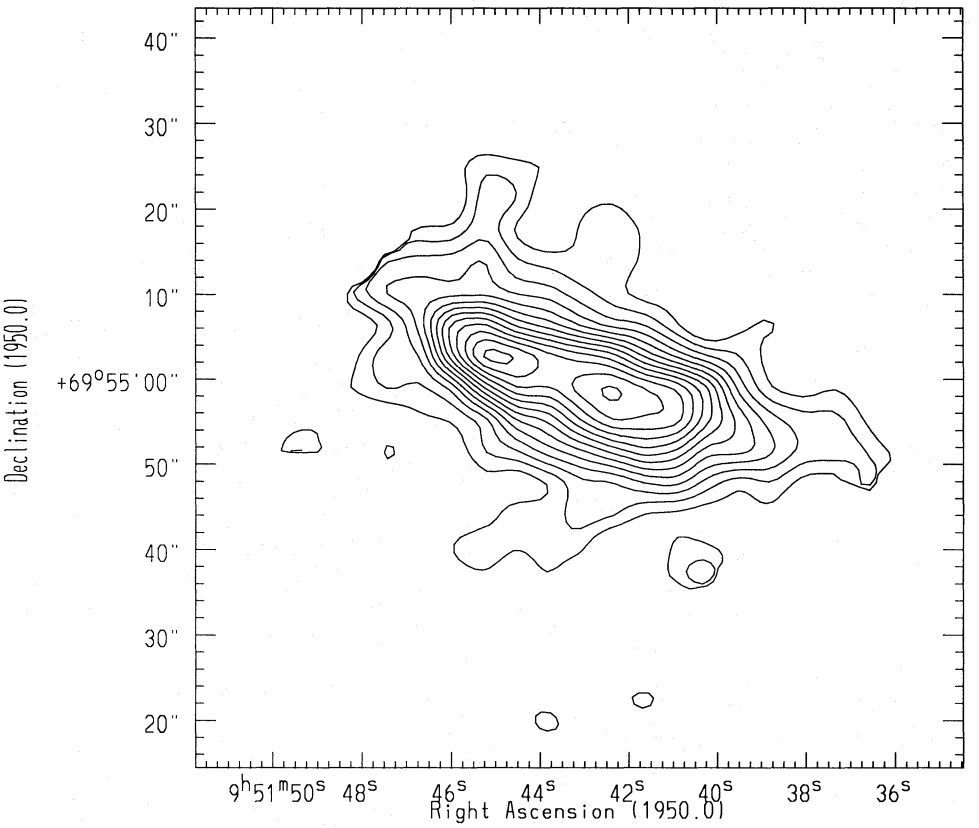

Figure 1. A diffraction-limited continuum map at 450 μm of the nuclear region in M82. The noise level is 150 mJy beam^{-1}. The lowest level contour shown is 300 mJy beam^{-1} with a contour interval of 300 mJy beam^{-1}. The mean beamsize is 9 arcsec FWHM.

performed against Mars assuming a brightness temperature of ~208 K. The purpose of making the NRAO 12-m measurements was to provide integrated fluxes over the central 1 kpc (~65 arcsec) of M82 to compare directly with those obtained at shorter millimetre and submillimetre wavelengths (Paper I; Krügel et al. 1990).

A large-single-beam measurement (0.65 ± 0.08 Jy) was made at 3 mm (θ_b ~ 75 arcsec HPBW) and agrees with an earlier large-beam flux density of 0.540 ± 0.083 Jy (Jura, Hobbs & Maran 1978). Due to the smaller beamsize at 2 mm (θ_b ~ 45 arcsec HPBW), it was necessary to make a three-point strip map, centred on the IR nucleus, along the major axis of M82. Fig. 2 shows the 2-mm continuum emission to be clearly resolved and, in order to estimate the total extended flux, some model must be applied to the data given in Table 1. A Gaussian profile with a peak flux density, F_{peak}, of 630 mJy and a beam-convolved source size, θ_{b*s}, of 57 arcsec provided a best fit to the data when offset 10 arcsec to the south-west of the IR nucleus. This shift places the 2-mm continuum peak in the vicinity of the secondary IR peak (Joy, Lester & Harvey 1987) and the most active star-forming region in M82 (Section 3.2). However, the structure of the central 1 kpc at 3.3 mm (Carlstrom & Kronberg 1991) and 1.3 mm (Krügel et al. 1990) shows an elongated ridge. An alternative approach is to model the source with a flat-topped disc intensity distribution.

In the Gaussian model, for a HPBW $\theta_b = 45$ arcsec, we determine a deconvolved source size $\theta_s = 34$ arcsec which is in good agreement with the measurements at other submillimetre and millimetre wavelengths (see Section 3.4.1), and an integrated 2-mm flux density, F_{tot}, of 1.0 ± 0.2 Jy assuming that

$$F_{tot} = [1 + (\theta_s/\theta_b)^2] F_{peak}, \quad (1)$$

where $\theta_s = (\theta_{b*s}^2 - \theta_b^2)^{1/2}$.

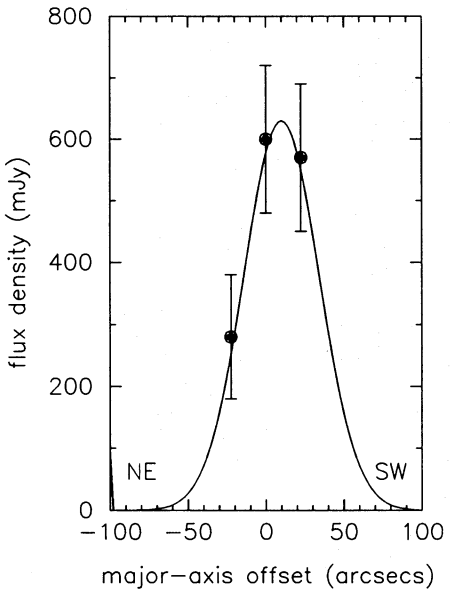

Figure 2. A 2-mm continuum strip map of M82 along the major axis at a PA of 72°. The positional offsets are with respect to the IR nucleus [$\alpha(1950.0) = 09^h\ 51^m\ 43\overset{s}{.}53$, $\delta(1950.0) = 69°\ 55'\ 00\overset{''}{.}7$ (Dietz et al. 1986)]. The solid line shows the best fit to the data assuming a Gaussian source (see Section 2.2) with an offset of the peak intensity 10 arcsec to the south-west of the IR nucleus and a beam-convolved source size of 57 arcsec (FWHM).

In the disc model, for a ridge of length R extending 40 arcsec and peaking at a flux level of ~600 mJy, we calculate an integrated 2-mm flux density of 0.8 ± 0.1 Jy, assuming in this instance that

$$F_{tot} = \frac{x^2}{1 - \exp(-x^2)} F_{peak}, \quad (2)$$

where $x = 0.84\, R/\theta_b$ (Baars 1973).

It is concluded that M82 has an integrated 2-mm flux density of 0.9 ± 0.2 Jy, where the error reflects the uncertainty in the model fitting and not the statistical error of the data. The results of all millimetre and submillimetre mapping are summarized in Table 2, and a discussion of the FIR–millimetre spectral energy distribution is deferred to Section 3.5.

3 RESULTS AND DISCUSSION

The most striking result from these observations is that the 450-μm continuum emission shows a double-peaked structure (Fig. 1), which differs from that of an earlier 450-μm map at lower resolution (Smith et al. 1990), and is similar to that observed in the continuum at all mid-IR and FIR wavelengths (Rieke et al. 1980; Joy et al. 1987; Dietz et al. 1989; Telesco et al. 1991) where thermal reradiation from heated dust grains dominates the observed luminosity. A double-lobed structure is also consistent with the distribution of CO emission in a number of isotopes and differing transitions (Lo et al. 1987; Loiseau et al. 1988; Phillips & Mampaso 1989; Tilanus et al. 1991). The low surface brightness contours at 450 μm show spurs and extensions which, although close to the noise level, find counterparts in the mid-IR (Telesco et al. 1991) and CO maps (Nakai et al. 1987; Loiseau et al. 1990), supporting our conclusion that they are real. The good spatial correspondence of these

Table 1. 2.14-mm NRAO observations.

offset[a] (arcsecs)	beam position (epoch 1950.0)	flux density[b] (mJy)
(0, 0)	(09 51 43.8, +69 54 59)	600 ± 56
(−22.5, 0)	(09 51 39.7, +69 54 53)	570 ± 56
(+22.5, 0)	(09 51 47.5, +69 55 08)	280 ± 48

[a]Offset from the IR nucleus (0, 0) along the major axis at a PA of 72°.
[b]Flux density in a 45-arcsec beam.

Table 2. Summary of submillimetre and millimetre mapping data.

Wavelength	flux density (Jy)	mapped region
450 μm[1]	41 ± 6	68″ × 68″
450 μm[2]	49 ± 21	40″ × 40″
800 μm[3]	4.9 ± 0.7	74″ × 74″
1100 μm[3]	2.4 ± 0.4	80″ × 90″
1300 μm[4]	2.1 ± 0.2	180″ × 120″
2.14 mm[1]	0.9 ± 0.2	strip-map (45″ HPBW)
3.3 mm[1]	0.65 ± 0.08	single beam (75″ HPBW)
3.3 mm[5]	0.59 ± 0.09	120″ × 120″

References: (1) this paper; (2) Smith et al. (1990); (3) Hughes et al. (1990); (4) Krügel et al. (1990); (5) Carlstrom & Kronberg (1991).

features in the dust continuum and molecular lines is discussed below. In the following sections we consider the wavelength-dependent structure of M82, bearing in mind the uncertainties in the absolute positional accuracy (~ 3 arcsec) of continuum and spectral line maps. We also describe the evidence for a temperature and density gradient within the dust torus, and update our discussion in Paper I of the integrated FIR–millimetre spectrum, taking advantage of maps at 1.3 mm (Krügel et al. 1990) and at 3.3 mm (Carlstrom & Kronberg 1991) in addition to the new data presented here.

3.1 High surface brightness features

The centroids of 450-μm peak emission are symmetrically placed about the IR nucleus to within the positional accuracy of the map. The north-eastern peak is at a position $\alpha(1950.0) = 09^h\ 51^m\ 44\overset{s}{.}85$, $\delta(1950.0) = 69°\ 55'\ 02\overset{''}{.}5$, and the south-western peak is at a position $\alpha(1950.0) = 09^h\ 51^m\ 42\overset{s}{.}33$, $\delta(1950.0) = 69°\ 54'\ 58\overset{''}{.}5$. The submillimetre peaks of emission (i) are separated by 15 ± 2 arcsec (230 pc), (ii) are further apart than observed in the mid-IR (10 ± 1 arcsec: Telesco et al. 1991) and (iii) are situated more towards the inner edges of the two bright ^{12}CO(1–0) peaks (Carlstrom 1988) that define the limb-brightened edge-on molecular torus. It is probable that the sensitivity and asymmetric beam profile of the 450-μm data prevent us from resolving the south-western peak into the two structures associated with the western lobe and the central clump seen in the higher resolution ^{12}CO(1–0) map. Rieke et al. (1980), with higher resolution (2.5 arcsec) observations, and Dietz et al. (1989), using a maximum entropy algorithm, have resolved the south-western peak at 10 μm into two separate sources. Unfortunately, Dietz et al. do not show the result of a maximum entropy analysis performed on their 20-μm data. The 450-μm peaks have equal brightnesses, whereas at mid-IR wavelengths (10–30 μm) the continuum emission from the south-western peak is found to be ~ 20 per cent brighter than that from the north-eastern peak.

3.2 Low surface brightness features

The major axis of the 450-μm emission (Fig. 1) has a position angle (PA) of 72° for the central ridge and rotates to a PA = 66° at lower surface brightness levels. This offset is close to the difference in values of 4° between the PA of the infrared nuclear bar (70°) and that of the more extended 2.2-μm emission (Telesco et al. 1991). The overall extent of the 450-μm emission defined by the 3σ contour is $\sim 65 \times 25$ arcsec^2 and cuts off exactly at the end of the IR bar, providing further evidence that the presence of a nuclear stellar bar and the formation of a massive dust and gas torus are closely associated with the active burst of nuclear star formation observed within the central 750 pc.

In Paper I we suggested that dust grains, driven outwards from the nucleus by the mechanical energy provided by the many supernova events (Kronberg, Biermann & Schwab 1981; Kronberg et al. 1985) and OB stars (O'Connell & Mangano 1978), pile up as they encounter the molecular cylinder or thick torus (Nakai et al. 1987) that is presumed to collimate the observed X-ray (Watson et al. 1984) and Hα (McCarthy et al. 1987; Bland & Tully 1988) outflows. The 800-μm map (Paper I) allowed the speculation that enhancements in the grain distribution were observed perpendicular to the plane and interior to the putative molecular collimating walls. The higher resolution 450-μm data presented here provide more convincing evidence (see Fig. 3a). If this picture is correct, however, it appears that the molecular and grain density enhancement in the western wall is significantly weaker than in the eastern wall. Fig. 3(b) shows that the eastern low surface brightness spur could define a perpendicular wall that constrains the X-ray outflow in that region. A possible reason why the western wall is less clearly defined in the 450-μm and CO data is described below.

In Fig. 3(c) we show a schematic picture of the major features in the nucleus of M82 (adapted from Joy et al. 1987) superimposed on the 450-μm map. The western 450-μm peak (which is resolved into two sources at 10 μm) is centred on the most active region in the starburst nucleus. Within 100 pc are the secondary IR peak (Joy et al. 1987; Telesco et al. 1991), the brightest supernova remnant 41.9 + 58 (Kronberg et al. 1981) and a number of OH masers (Weliachew et al. 1984) usually associated with massive star-forming regions. Kronberg et al. (1981) noted two radio jet-like ridges projecting 15 arcsec westward from 41.9 + 58 and the maser sources. The 450-μm, 10-μm, X-ray and CO data all show the same linear feature extending 30 arcsec west of the active region, which includes a small cluster of five compact VLA radio sources which may provide a source of local heating and outflow. The overall distribution of the compact radio sources to the south-west of the IR nucleus shows a tendency to be more extended, as well as ~ 90 per cent brighter than to the north-east (see Fig. 3d). Whilst the overall optical emission shows an irregular structure with variable obscuration due to dust, the optical *B*-band image by O'Connell & Mangano (1978) provides further evidence for greater activity from young stars extending > 45 arcsec west of the IR nucleus. Also, the outflowing material seen in Hα and X-rays shows a prominent spur displaced to the west of the primary IR nucleus and extending south from the Galactic plane (Section 3.3). The spur appears to be driven outwards from the highly active region described above. It is therefore possible that the collimating western wall has been severely disturbed or broken through as a result of the proximity of the active region.

Alternatively, the CO emission may not arise from a toroidal distribution at all. Lo et al. (1987) have argued, on the basis of morphological and kinematic evidence, that the observed distribution of CO implies that the molecular gas in M82 is highly disturbed and cannot be due to a simple rotating torus viewed edge-on. The asymmetry in the distribution of the ^{12}CO emission about the IR nucleus and the variation in the position angles of the western and eastern lobes are confirmed in the CO map by Carlstrom & Kronberg (1991). Brouillet & Schilke (1993) have made high-resolution (3 arcsec) HCN(1–0) observations of M82, and have resolved the putative molecular ring into a number of massive clumps (~ 10^6 $M_\odot$) and also found a component in the rotation curve suggesting solid-body rotation.

3.3 The southern spur

In Paper I it was claimed that at 1.1 mm a spur of thermal dust emission was found extending to the south of the galaxy, possibly associated with the similar plumes of material detected in Hα (McCarthy et al. 1987) and X-ray emission

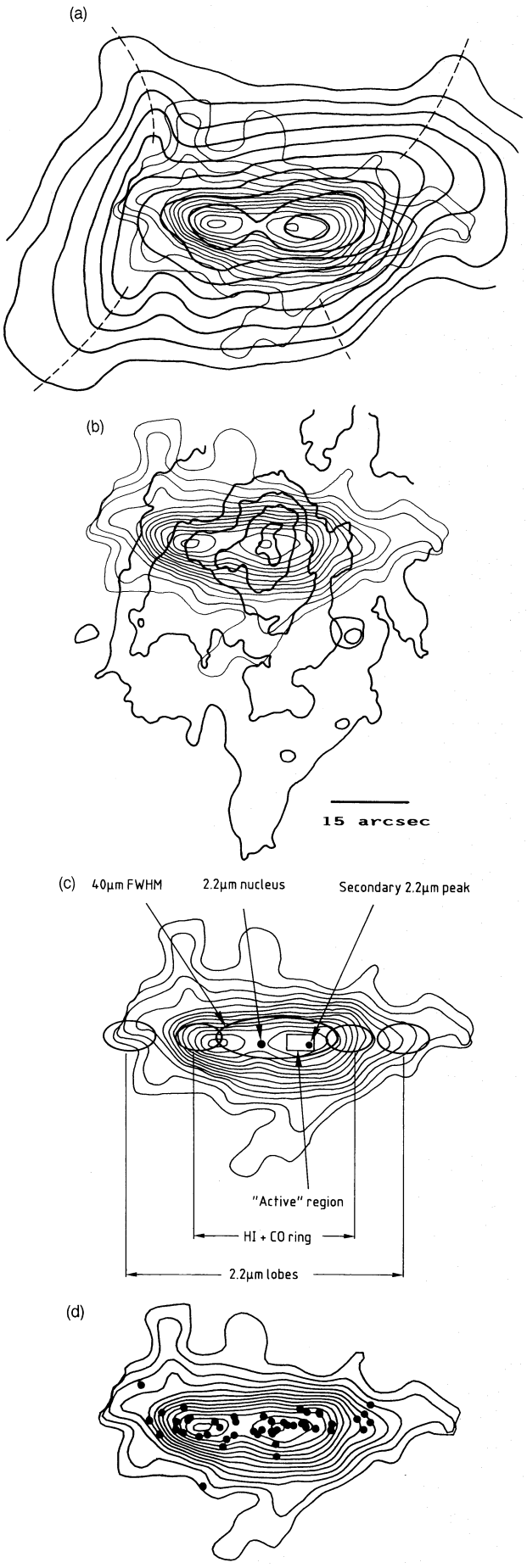

Figure 3. A comparison of the 450-μm continuum emission with (a) ^{12}CO(1–0) emission (Nakai et al. 1987) showing the putative perpendicular collimating wall (dashed lines), (b) X-ray emission (Watson et al. 1984) illustrating the confinement of the X-ray emission east of the nucleus and the southern spur, (c) an overlay of the major nuclear features (adapted from Joy et al. 1987) showing the coincidence of the *active* region, in particular the secondary near-IR peak, with the western 450-μm lobe, (d) the positions of the compact VLA radio sources (Kronberg et al. 1985; Huang et al. 1994).

(Watson et al. 1984). Extended emission at the same position has also been detected in the ^{12}CO(2–1) (Loiseau et al. 1990) and HCN(1–0) maps (Brouillet & Shilke 1993) at velocities of ~ 170 km s^{-1} with respect to the centre of the galaxy. The reality of this feature was disputed by Krügel et al. (1990), although the spur is again seen in the high-resolution 450-μm data presented here (Fig. 1).

The 450-μm data were smoothed to an effective resolution of 11 arcsec (Fig. 4) to compare directly with the 1.3-mm map by Krügel et al. Whilst the southern spur appears only weakly at this resolution, the close spatial agreement in both the high and low surface brightness features implies that both the 450-μm and 1.3-mm emissions arise from the same grains. It is important to establish this fact before an isothermal spectrum is fitted to the FIR–millimetre spectral energy distribution (Section 3.5).

3.4 A toroidal temperature and density gradient

3.4.1 Source size as a function of wavelength

The straightforward interpretation of the new 450-μm data is that they represent a cooler component ($T \sim 50$ K) of the dusty edge-on torus already detected at mid-IR wavelengths ($T \sim 150$ K). The dust grains radiating at submillimetre wavelengths are more likely to be associated with the dense molecular gas, whilst the grains emitting at mid-IR wavelengths lie predominantly at the hotter interface of the ionized and molecular phases. The larger separation of the peaks at 450 μm reflects the radial temperature gradient that must exist within the torus if the dust is heated by the central starburst population, regardless of whether the nucleus is a point source or extended. This result is quantified in Table 3 and in Fig. 5, where we present the beam-deconvolved source sizes along the major and minor axes for all continuum maps between 10 μm and 3.3 mm.

The dust torus in M82 shows a constant source size (~ 8 arcsec FWHM, 126 pc) perpendicular to the galactic plane. In contrast, good evidence for a trend of increasing source

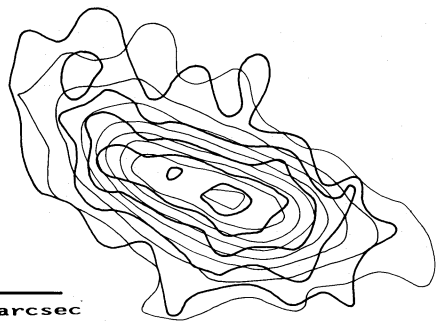

Figure 4. 450-μm data (light line) smoothed to 11-arcsec resolution and compared to the 1.3-mm data (heavy line) (Krügel et al. 1990).

size with increasing wavelength for 10 μm < λ < 1.3 mm is seen within the plane. This result indicates that no significant temperature gradient exists along the minor axis, in contrast to a decrease in the dust temperature with increasing distance from the nucleus along the major axis. For λ > 1 mm the contribution from free–free emission is > 20 per cent, and this artificial enhancement in the observed peak flux produces the effect of decreasing the measured FWHM source size and hence the turnover in the overall trend for λ > 1.3 mm seen in Fig. 5.

Table 3. Deconvolved source sizes in M82.

Wavelength	beam-size (FWHM)	major-axis (″)	minor-axis (″)
10.8μm	3.9″ × 4.2″	24	7
19.2μm	3.9″ × 4.2″	28	9
30μm	4.7″ × 5.0″	24	5
40μm	14″	25	8
58μm	18″	30	–
100μm	24″	35	14
450μm	9″	35	9
800μm	14″	40	8
1.1 mm	22″	37	< 22[a]
1.3 mm	11″	38	9
2.14 mm	45″	34	–
3.35 mm	6.1″ × 6.9″	21	6

[a]Unresolved along the minor axis at 1.1 mm.

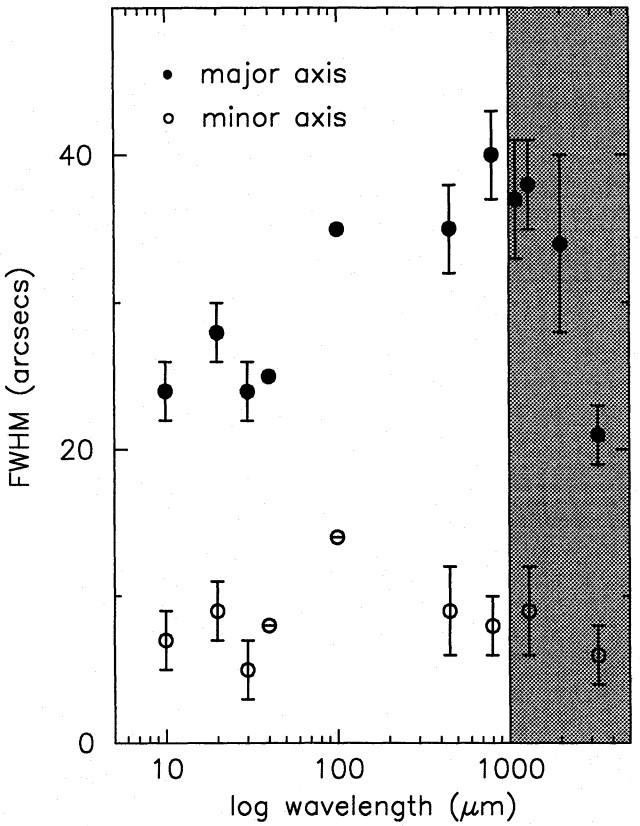

Figure 5. Deconvolved source size as a function of wavelength. The data for the minor axis (open circles) show no evidence for change in source size with wavelength, in contrast to the major axis (solid circles) where the trend suggests that the dust temperature decreases with increasing distance from the IR starburst nucleus. The shaded region shows the wavelength regime (λ > 1 mm) in which free–free emission contributes > 20 per cent to the total flux.

3.4.2 *450-μm major-axis intensity profile*

The 450-μm continuum map cannot provide any dynamical evidence for a toroidal distribution of the dust. However, a simple model of an edge-on torus with appropriate temperature and density distributions is consistent with the observed 450-μm intensity slice taken along the major axis.

A model of the thermal emission from dust in an optically thin torus was constructed, and integration was performed along the major axis as if viewed edge-on assuming a grain sublimation temperature of 1800 K, a radial temperature distribution $T(r) \propto r^{-0.4}$ and an inner radius of 6 arcsec (95 pc). The model profile was convolved with a 9-arcsec Gaussian, and both the model and the observed 450-μm data were normalized to allow comparison. Fig. 6 shows that good agreement between the model and the data was found for a density profile $n(r) \propto r^{-\gamma}$ with $\gamma \sim 0.6$–1.0. The largest deviation between the model and data is found at > 15 arcsec south-west of the IR nucleus, where it has already been suggested (Section 3.2) that disruption of the dusty molecular collimating torus may have occurred as the result of increased star-forming activity in the region.

3.5 Decomposition of the radio–FIR spectral energy distribution (SED)

3.5.1 *3 mm–40 μm SED*

The subtraction of an optically thin free–free spectrum (i.e. $F_\nu \propto \nu^{-0.1}$) with a flux of 0.59 Jy at 3.35 mm leaves the residual 40 μm–3.3 mm data (shown in Fig. 7) which were modelled with an isothermal 48-K greybody function,

$$F_\nu = \Omega B_\nu(T)\left\{1 - \exp\left[-\left(\frac{\lambda_0}{\lambda}\right)^\beta\right]\right\}, \quad (3)$$

solving for the solid angle (Ω), the dust temperature (T), the emissivity power-law exponent of the grains (β) and the wavelength at which the optical depth is unity (λ_0). The best-fitting parameters are given in Table 4, and the solid line in Fig. 7 shows the $T = 48$ K model spectrum. This dust temperature and emissivity index ($\beta = 1.3$) differ from the values favoured by Krügel et al. (1990), who argue that the observed variation in source size with wavelength between 40 μm and 1.3 mm and the possible variation of β with wavelength make the determination of T and β difficult. Instead, they adopt the mean temperature of $T = 30 \pm 5$ K and $\beta = 2 \pm 0.2$ derived for a sample of Markarian galaxies (Chini et al. 1989).

The source size between 100 μm and 1.3 mm (Fig. 5) is roughly constant (37 × 10 arcsec² FWHM), and provides some a priori information on the solid angle of the FIR–millimetre emission region which appears to be tracing the same temperature component at these wavelengths. Hence only the 3.3 mm–100 μm data were included in a second fit in which the dust temperature and solid angle were forced to take the values $T = 30$ K and Ω = 370 arcsec²

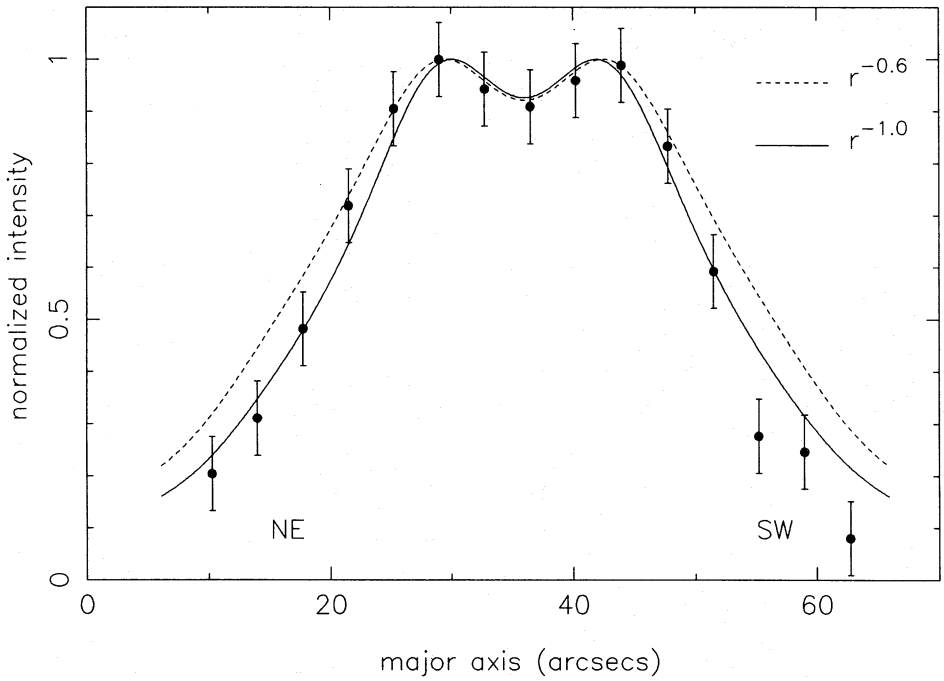

Figure 6. A major-axis profile at 450 μm normalized to the peak flux is compared to the model profile, smoothed with a 9-arcsec Gaussian, due to thermal emission from dust in an optically thin edge-on torus. Two density distributions $n(r) \propto r^{-\gamma}$ in the torus, i.e. $\gamma = 0.6$ and 1.0, are represented by dashed and solid lines respectively.

Table 4. Isothermal greybody model: best-fitting parameters for the 40 μm–3.3 mm data after the subtraction of a free-free spectrum.

T	48.1 K
β	1.3
Ω	1.34×10^{-8} ster.
θ^a	27″ (425 pc)
$\lambda_0(\tau = 1)$	$7.9 \mu m$
A_V^b	50
χ^2_ν	1.7
M_d	1.8×10^6 M$_\odot$

[a]Source size $\theta_s = 2(\Omega/\pi)^{1/2}$.
[b]$A_{8\,\mu m}/A_V = 0.020$ (Rieke & Lebofsky 1985).

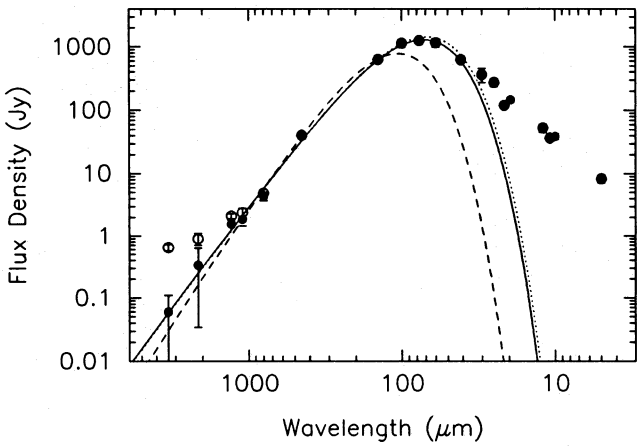

Figure 7. Residual mid-IR to millimetre spectral energy distribution (solid circles) after the subtraction of an optically thin free–free continuum spectrum (0.59 Jy at 3.35 mm). The open circles represent the uncorrected data. The solid curve shows the isothermal ($T = 48$ K) greybody model with all parameters (Ω, T, β, λ_0) fitted freely to the 40 μm–3.3 mm data. The dotted and dashed curves illustrate the fits to the 100 μm–3.3 mm data only. The dashed curve shows the best fit with both the source solid angle ($\Omega = 370$ arcsec^2) and the dust temperature ($T = 30$ K) constrained. In the case of the dotted curve, only the solid angle is fixed ($\Omega = 370$ arcsec^2), resulting in a best-fitting temperature of 50 K.

$(8.7 \times 10^{-9}$ sr) whilst allowing the remaining parameters ($\beta = 1.8$, $\lambda_0 = 51$ μm) to be freely determined with $\chi^2_\nu = 2.6$. For comparison, the fit was repeated with the dust temperature also as a free parameter, and a best fit ($\chi^2_\nu = 1.7$) was obtained for a 50-K greybody with $\beta = 1.3$ and $\lambda_0 = 11.1$ μm. This latter result provides an acceptable fit between 100 and 40 μm. Both results are also shown in Fig. 7. More importantly, if the average values of the 1–13 μm extinction law (Rieke & Lebofsky 1985) are used, then the hotter models imply a visual optical depth of $A_V = 17$–50. This range of values is consistent with $A_V = 27 \pm 4$ determined from the reddening-insensitive measurement of the H53α recombination line (Puxley et al. 1989) and $A_V = 41$ from the radiative transfer model by Krügel & Siebenmorgen (1994), whilst the colder ($T = 30$ K) dust model predicts an $A_V \geqq 50$.

It is clear from this discussion, however, that the temperature of the dust that causes the FIR spectral cut-off is between 30 and 50 K, although we prefer the ~50-K model

for the reasons already given. The requirement for hotter dust to explain the mid-IR data is described in Section 3.5.2.

An estimate of the dust mass in the central 1 kpc of the starburst nucleus of M82 at a distance $D = 3.25$ Mpc was made using the relationship

$$M_{\rm d} = \frac{F_\nu D^2}{k_{\rm d} B_\nu(T)}. \tag{4}$$

The grain mass absorption coefficient $k_{\rm d} = 3\,Q_\nu/4a\rho$, where a and ρ are the grain radius and density respectively, is not well defined at submillimetre wavelengths, since it depends primarily on the uncertainty of the grain emission efficiency, Q_ν (Draine 1990). A dust mass of 1.8×10^6 $M_\odot$ is calculated from the 450-μm flux of 41 Jy and the parameters in Table 4, assuming a value of $k_{\rm d}^{450\,\mu{\rm m}} = 0.246$ m^2 kg^{-1}, and is only a factor of 2 larger (3.66×10^6 $M_\odot$) if the best-fitting parameters for the lower temperature model ($T = 30$ K) are used.

3.5.2 *Mid-IR spectral energy distribution*

Thermal emission from dust grains radiating over a broad range of temperatures (1500–20 K) can show a characteristic quasi-power-law spectrum at IR–FIR wavelengths ($3 < \lambda < 100$ μm), where the spectral index depends on the density structure ($\mathrm{d}N/\mathrm{d}r$) and temperature structure ($\mathrm{d}T/\mathrm{d}r$) as well as on variations in the emission efficiency of the grains with wavelength within the emitting region.

Rees et al. (1969) and Bollea & Cavaliere (1976) have described the simple case of optically thin IR emission, for which the radiated flux from a spherical distribution of grains surrounding and heated by a strong central UV radiation field is given by

$$F_\nu \propto \int Q_{\rm IR} B_\nu(T) \frac{\mathrm{d}N}{\mathrm{d}T} \mathrm{d}T, \tag{5}$$

where $\mathrm{d}N/\mathrm{d}T$ represents the temperature distribution of the grains. Assuming that the radial dependence of the number density can be expressed as a power law, i.e. $n(r) \propto r^{-\gamma}$, then

$$\frac{\mathrm{d}N}{\mathrm{d}r} \propto r^{2-\gamma} \tag{6}$$

and

$$\frac{\mathrm{d}T}{\mathrm{d}r} \propto r^{-(6+\beta)/(4+\beta)}. \tag{7}$$

Combining these expressions to determine $\mathrm{d}N/\mathrm{d}T$, it follows that if the spectral energy distribution at mid-IR wavelengths approximates a power law $F_\nu \propto \nu^\alpha$ then the mid-IR spectral index

$$\alpha_{\rm IR} = -[2 + (4+\beta)(1-\gamma)]/2. \tag{8}$$

In M82, $\alpha_{\rm IR} \simeq -2$ and hence, for $\beta \sim 1$–2 (Section 3.5.1), the radial distribution of grains has some central concentration with $n(r) \propto r^{-0.6}$. This is an independent measure of the density structure, which is consistent with that required to fit the intensity profile at 450 μm along the major axis (Section 3.4.2). This result is also in agreement with the radiative transfer model by Krügel & Siebenmorgen (1994).

4 CONCLUSIONS

(1) The structure of the 450-μm continuum emission shows two peaks of equal brightness separated by 15 arcsec. The observed major-axis intensity profile can be adequately modelled with thermal dust emission from an edge-on torus heated by the nuclear starburst region. Within their respective positional uncertainties, the 450-μm peaks lie outside the mid-IR peaks and on the inner edge of the larger scale CO molecular torus.

(2) The size of the continuum emitting region increases with wavelength between 10 μm and 1.3 mm, and suggests that a temperature gradient must exist throughout the torus.

(3) The low surface brightness 450-μm emission shows spurs that are perpendicular to the plane of the galaxy and appear to be associated with the putative molecular cylinder. The simple cylindrical geometry of this collimating material, however, may have been dynamically disturbed by the increased star-forming activity towards the south-western half of the galaxy.

(4) We find evidence for a southern extension at 450 μm that appears to originate from the active south-western peak and is co-spatial with the observed X-ray and Hα outflowing material.

(5) An isothermal greybody model ($T = 48$ K, $\beta = 1.3$, $\lambda_0 = 8$ μm, $\theta_{\rm s} = 27$ arcsec) is fitted to the residual 3.3 mm–40 μm data after the subtraction of bremsstrahlung emission (0.59 ± 0.05 Jy at 3.35 mm). The source size and optical depth are consistent with observations. A dust mass of 1.8×10^6 $M_\odot$ is calculated within the central 1 kpc.

Until the absolute positional accuracy and registration between maps are better than 1 arcsec, it will remain difficult to determine whether the difference in the relative positions of the continuum and molecular line maxima at different wavelengths implies a genuine lack of physical association between certain features, a temperature gradient or the result of variations in the opacity of the material. This uncertainty in positional registration hinders many attempts to improve our understanding of the relationship between molecular and ionized gas, warm and hot dust, stars and supernova remnants in one of the nearest and best-studied starburst galaxies.

ACKNOWLEDGMENTS

We thank the JCMT staff at the Joint Astronomy Centre, Hilo, for their assistance in making these observations and, in particular, Goeran Sandell for his valuable advice during the reduction of these data. The JCMT is operated by The Observatories on behalf of the UK Particle Physics and Astronomy Research Council, the Netherlands Organization for Scientific Research (NWO) and the Canadian National Research Council. We also thank Phil Jewell and the telescope operators Ed and Lisa at the NRAO 12-m. The National Radio Astronomy Observatory is operated by Associated Universities, Inc., under cooperative agreement with the US National Science Foundation. This research has made use of the NASA/IPAC Extragalactic Database (NED) which is operated by the Jet Propulsion Laboratory, Caltech, under contract with the National Aeronautics and Space Administration. DHH gratefully acknowledges receipt of a PPARC PDRA during the course of this work.

REFERENCES

Axon D. J., Taylor K., 1978, Nat, 274, 37
Baars J. W. M., 1973, IEEE Trans. Antennas Propagation, AP-21, 461
Bland J., Tully R. B., 1988, Nat, 334, 43
Bollea D., Cavaliere A., 1976, A&A, 49, 313
Brouillet N., Schilke P., 1993, A&A, 277, 381
Burbidge E. M., Burbidge G. R., Rubin V. C., 1964, ApJ, 140, 942
Carlstrom J. E., 1988, in Dickman R., Snell R., Young J., eds, Molecular Clouds in the Milky Way and External Galaxies. Springer-Verlag, p. 405
Carlstrom J., Kronberg P. P., 1991, ApJ, 366, 422
Chini R., Krügel E., Kreysa E., Gemünd H. P., 1989, A&A, 216, L5
Dietz R. D., Gehrz R. D., Jones T. J., Grasdalen G. L., Smith J., Gullixson C., Hackwell J. A., 1989, AJ, 98, 1260
Draine B. T., 1990, in Thronson H. A., Shull J. M., eds, The Interstellar Medium in Galaxies. Kluwer, Dordrecht, p. 483
Duncan W. D., Robson E. I., Ade P. A. R., Griffin M. J., Sandell G., 1990, MNRAS, 243, 126
Huang Z. P., Thuan T. X., Chevalier R. A., Condon J. J., Yin Q. F., 1994, ApJ, 424, 114
Hughes D. H., Gear W. K., Robson E. I., 1990, MNRAS, 244, 759 (Paper I)
Joy M., Lester D. F., Harvey P. M., 1987, ApJ, 319, 314
Jura M., Hobbs R. W., Maran S. P., 1978, AJ, 83, 153
Kronberg P. P., Biermann P., Schwab F. R., 1981, ApJ, 246, 751
Kronberg P. P., Biermann P., Schwab F. R., 1985, ApJ, 291, 693
Krügel E., Siebenmorgen R., 1994, A&A, 282, 407
Krügel E., Chini R., Klein U., Lemke R., Wielebinski R., Zylka R., 1990, A&A, 240, 232
Lo K. Y., Cheung K. W., Masson C. R., Phillips T. G., Scott S. L., Woody D. P., 1987, ApJ, 312, 574
Loiseau N., Reuter H.-P., Wielebinski R., Klein U., 1988, A&A, 200, L1
Loiseau N., Nakai N., Sofue Y., Wielebinski R., Reuter H.-P., Klein U., 1990, A&A, 228, 331
McCarthy P. J., Heckman T., van Breugel W., 1987, AJ, 93, 264
Muxlow T. W. B., Pedlar A., Wilkinson P. N., Axon D. J., Sanders E. M., de Bruyn A. G., 1994, MNRAS, 266, 455
Nakai N., Hayashi M., Handa T., Sofue Y., Hasegawa T., 1987, PASJ, 39, 685
O'Connell R. W., Mangano J. J., 1978, ApJ, 221, 62
Phillips J. P., Mampaso A., 1989, A&A, 218, 24
Puxley P. J., Brand P. W. J. L., Moore T. J. T., Mountain C. M., Nakai N., Yamashita T., 1989, ApJ, 345, 163
Rees M. J., Silk J. I., Werner M. W., Wickramasinghe N. C., 1969, Nat, 223, 788
Richer J. S., Padman R., Ward-Thompson D., Hills R. E., Harris A. I., 1993, MNRAS, 262, 839
Rieke G., Lebofsky M. J., 1985, ApJ, 288, 618
Rieke G., Lebofsky M. J., Thompson R. I., Low F. J., Tokunaga A. T., 1980, ApJ, 238, 24
Smith P. A., Brand P. W. J. L., Puxley P. J., Mountain C. M., Nakai N., 1990, MNRAS, 243, 97
Tammann G. A., Sandage A. R., 1968, ApJ, 151, 835
Telesco C. M., Harper D. A., 1980, ApJ, 235, 392
Telesco C. M., Campins H., Joy M., Dietz K., Decher R., 1991, ApJ, 369, 135
Tilanus R. P. J., Tacconi L. J., Sutton E. C., Zhou S., Sanders D. B., Wynn-Williams C. G., Lo K. Y., Stephens S. A., 1991, ApJ, 376, 500
Watson M. G., Stanger V., Griffiths R. E., 1984, ApJ, 286, 144
Weliachew L., Fomalont E. B., Greisen E. W., 1984, A&A, 137, 335